THE JOURNAL OF PHYSICAL CHEMISTRY C

pubs.acs.org/JPCC Article

Time-Resolved Shadowgraph Photography of Laser-Heated Plasmonic Gold Nanoparticles in Water

Derek Stavich, Boris Nestoiter, Daniel Gonzalez, Adam Freund, Xavier Buelna, Kaiyue Wang, Joseph A. Teprovich, Jr., and Jussi Eloranta*

Cite This: J. Phys. Chem. C 2020, 124, 14022−14029 Read Online

ACCESS | Metrics & More | Article Recommendations | Supporting Information

ABSTRACT: Fragmentation and the subsequent heat transfer from solvated gold nanoparticles with sizes 50, 100, 150, and 250 nm to water are studied by time-resolved shadowgraph photography. The measured fragmentation thresholds indicate that the particles heat up to temperatures between the boiling point and critical temperature of gold. At high laser energy densities, complete fragmentation of the particles is observed, which is evidenced by the sudden breakdown of the thermally insulating Leidenfrost layer initially surrounding the laser-heated particles. The consequent heat transfer results in the production of water vapor, which expands through pressure−volume work to form a micrometer-sized bubble. The spatially resolved shadowgraph images of these bubbles show the exact locations of the parent nanoparticles in the solution. Furthermore, a simple thermodynamic model can be used to relate the observed maximum bubble diameters to the original nanoparticle sizes. Although the presented method for online analysis of plasmonic metal nanoparticles in the liquid phase is destructive, it can be implemented in practice to employ a single laser pulse with a small beam size to achieve only minimal perturbation of the sample.

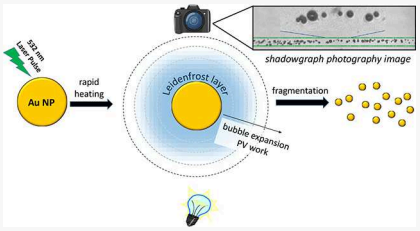

INTRODUCTION

Noble metal nanoparticles exhibit very intense size-dependent plasmon resonance absorption bands in the visible light and near-ultraviolet wavelengths.[1,2] Due to the large absorption cross section of these transitions, excitation with pulsed or continuous light sources results in efficient heating of the particles.[3−9] Laser heating of plasmonic nanoparticles plays an important role in many practical applications such as photocatalytic reactions,[10,11] solvothermal chemistry,[12] solar energy harvesting,[13,14] photothermal imaging,[15] and cancer therapy.[16]

In vacuum, particles can only dissipate the acquired energy through heat radiation, or at sufficiently high excitation energies they may melt and even undergo fragmentation due to boiling. In condensed medium (e.g., liquid water), heat transfer between the particle and the surrounding medium can take place, which results in the efficient production of heat near the particle. However, it has been established previously that the poor thermal conduction across the particle−water interface is due to the rapid appearance of an insulating Leidenfrost gas layer around the particle (also termed the Kapitza resistance[17] layer).[8,9,18−21] Thus, the overall heat transfer efficiency from the plasmonic nanoparticle to the surroundings is mostly determined by the physical characteristics of this dynamically evolving gas layer. When the local liquid temperature around the particle exceeds the boiling point, this layer would expand (i.e., surface tension and *P*ressure−*V*olume work) and produce a vapor bubble around the particle.

The optical study of bubbles formed around heated plasmonic nanoparticles in liquids is hindered by their small sizes under typical light exposure conditions.[6,7,22] Hence most of the recent studies have focused on metal nanoparticle arrays deposited on supporting substrates.[3,4,23−25] The vapor bubbles formed in such experiments overlap with multiple particles, which results in the appearance of a larger collective gas bubble. Since the particles are immobilized on the surface, continuous wave lasers can be conveniently used to study their formation mechanism and the resulting time evolution.

The direct study of vapor bubbles formed around individual laser-heated metal nanoparticles is less common. Application of spatially resolved optical imaging techniques (e.g., light scattering) is limited as the bubble sizes tend to be less than 1 μm and hence can be visualized only under high-power microscopes.[7] This makes it difficult not only to study larger bulk liquid samples but also to accurately analyze the time evolution of the vapor bubble. Combining these experimental studies with theoretical modeling, the elementary steps of the process have been established:[18,26,27] (1) plasmonic heating of the particle (possibly above the melting temperature), (2) particle to liquid heat transfer, (3) vapor formation around the

Received: March 25, 2020
Revised: June 4, 2020
Published: June 5, 2020

https://dx.doi.org/10.1021/acs.jpcc.0c02637
J. Phys. Chem. C 2020, 124, 14022−14029

particle (Leidenfrost layer), and (4) vapor expansion. The first three steps were suggested to proceed in the subnanosecond regime, but the last step can extend to longer time scales depending on the laser pulse characteristics. The developed theoretical models consider each of these steps and aim at obtaining the full dynamic description of the system.

The present study was inspired by our previous experiments on plasmonic copper and silver nanoparticles solvated in superfluid helium at 1.8 K temperature.[28] Due to the small vapor pressure of the liquid as well as the lowest known enthalpy of vaporization, the vapor bubbles formed around the metal nanoparticles grew to several tens of micrometers. Such bubbles were relatively easy to image (e.g., shadowgraph and Schlieren methods[29]) using modest optical magnification, which allows bulk liquid samples to be studied without any difficulty. In addition to allowing for time-resolved study of the system in the nanosecond time regime, the maximum semistationary bubble sizes could be determined. Instead of attempting to analyze the full trajectory of events theoretically, a simpler thermodynamic model, which considers only the incipient (initial) and fully extended bubble (final) states, was introduced. By calculating the amount of light absorbed by the particles using Mie theory,[28] it was possible to relate the fully extended gas bubble size to the parent nanoparticle size. Thus, the method allowed for determining not only the spatial locations of the individual particles but also their sizes in the liquid phase. Unfortunately, the amount of energy absorbed by the particles was well above their fragmentation threshold, which implies that the measurement was destructive.

The relationship between the maximum gas bubble radius and the nanoparticle size depends on several factors:[28] (1) the external pressure (expanding bubbles do *PV*-work), (2) the excitation wavelength (photon energy), (3) the complex dielectric response of the particle and the solvent, (4) the excitation photon flux (number of photons), and (5) the conversion efficiency of heat to *PV*-work. The first and last factors are expected to be smaller for water as compared to liquid helium experiments where the external pressure was around 10 torr at 1.7 K. While the conversion efficiency is an intrinsic property of the system, the external pressure can be reduced by pumping on the liquid vapors. As we show in this work, the vapor bubbles resulting from the laser excitation of aqueous gold nanoparticles grow sufficiently large that they can be directly observed by time-resolved shadowgraph photography employing only modest optical magnification.

Since the previous experiments with Cu and Ag nanoparticles in superfluid helium indicate that the high-power laser-heating process is destructive, we will first establish the laser-induced breakdown limits (i.e., single laser pulse optical bleaching) for aqueous gold nanoparticles as a function of their size. The trend observed in the bleaching thresholds can be explained using elementary thermodynamic modeling. By increasing the heating laser pulse energy well above the breakdown limit, we will then study the formation of vapor bubbles resulting from a complete nanoparticle breakdown process by time-resolved shadowgraph photography. The systematic connection between the presence of solvated gold nanoparticles and the appearance of micrometer-scale vapor bubbles induced by pulsed laser heating is confirmed by varying the particle concentration. In the next stage, by considering various gold nanoparticle sizes, the previously developed relationship[28] between the vapor bubble and parent nanoparticle sizes is verified based on the experimental data. It is shown that this method, albeit destructive, allows for the online detection of individual nanoparticle positions and sizes in a biologically relevant medium like bulk water.

EXPERIMENTAL SECTION

The stock samples were prepared from commercially available citrate buffer stabilized gold nanoparticle water solutions with nominal particle diameters 50, 100, 150, and 250 nm (Sigma-Aldrich). These samples were first analyzed by using the dynamic light scattering (DLS; NanoBrook Omni by Brookhaven Instruments) technique to verify uniform particle size distribution according to the manufacturer tolerance (<12% variability). The stock samples were then diluted using Millipore quality water to achieve the desired particle concentration inside a 1 cm long disposable poly(methyl acrylate) UV/vis cuvette (transparent down to 285 nm). To reduce the pressure inside the cuvette, the open end was connected to a two-stage mechanical vacuum pump (Leybold Trivac) equipped with an oil filter (Nor-Cal Products model C-0589-20167-1) by using a vacuum tight rubber adapter. The vapor pressure near the cuvette entrance was monitored with a capacitance manometer (MKS Baratron model 623), and the data were read by a digital multimeter (Agilent 34401A). The desired vapor pressure inside the cuvette was adjusted by a throttle valve (MKS Exhaust Valve Controller model 252A) placed between the cuvette entrance and the vacuum pump. Samples were initially pumped down to ca. 33 torr pressure and then allowed to degas for at least 30 min in order to eliminate the possible formation of transient gas bubbles in the solution. According to the water equation of state at 33 torr the boiling point is 303.7 K. Since the measurements were performed at room temperature (295 K), water is close to its boiling point. This will both minimize the energy spent on *PV*-work as well as heating and vaporizing the surrounding water.

The experiments employed a pulsed Q-switched Nd:YAG laser (Surelite-II, Continuum, Inc.) with a Gaussian pulse length of 5 ns and repetition rate of 10 Hz. The fundamental wavelength of the laser was first frequency doubled to 532 nm and then attenuated to the desired pulse energy by using a set of neutral density filters (N-BK7 R-Variant, Thorlabs, Inc.). The resulting pulse energy of the laser was measured by a power meter (Gentec Electro-Optique, Inc. model QE25SP-H-MB-DO) connected to a digital oscilloscope (Agilent DSO3062A). By using a set of precision drilled holes, the spatial laser beam profile was determined to be Gaussian with a full-width at half-maximum (fwhm) of 4 mm. In some experiments the laser beam was focused to the center of the sample cuvette by using a 24 mm focal length planoconvex lens (1.25 mm diam.). The focused-down laser beam width at the center of the cuvette was determined to be 50 μm by visualizing the scattered light profile from the nanoparticles. After a specified delay time following the heating laser pulse, a shadowgraph image was recorded from the focal area of the laser beam. The shadowgraph measurement employed a regular light-emitting diode (LED, emission band centered around 620 nm) as the backlight source, which was driven by a 90 ns long 15 V pulse to yield light output of approximately the same duration, and a monochrome charge coupled device (CCD) camera (ImagingSource model DMK 23U445) equipped with global shutter. The image was magnified by using a pair of matched lenses (achromat pair 1:1 with identical 30 mm focal lengths; Edmund Optics; working distance 2 cm and focal plane depth 10 μm), which yielded a

https://dx.doi.org/10.1021/acs.jpcc.0c02637
J. Phys. Chem. C 2020, 124, 14022−14029

spatial resolution of 0.872 pixels/μm at the focal plane. The spatial scale was calibrated using a test target with known reference marks. To eliminate the scattered laser light, a 550 nm long-pass filter (FSQ-OG550, Newport, Inc.) was placed in front of the imaging lens. An overview of the experimental setup is depicted in Figure 1.

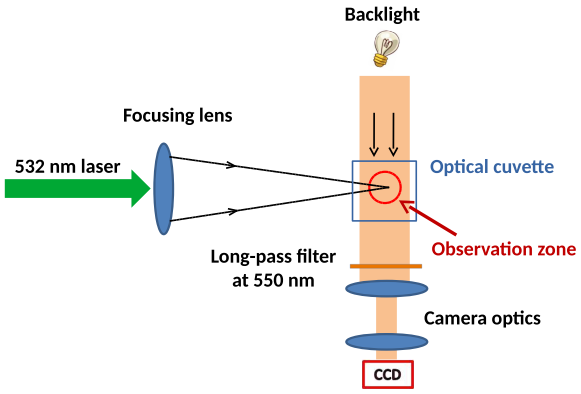

Figure 1. Experimental setup. "Observation zone" indicates the area where the gold nanoparticles are imaged.

The timing between the heating laser pulse and the shadowgraph backlight exposure was controlled by a digital delay generator (BNC model 565 Pulse Delay Generator) with a time jitter less than ±1 ns. The 2.4 V output pulse from the delay generator was amplified for the backlight LED by using the fast amplifier circuit described previously.[30] The delay generator and the CCD camera were both controlled by Raspberry Pi 3 computer using the libmeas software library.[31] Since the effective exposure time is determined by the backlight source operating in the nanosecond range, the slow CCD shutter was kept open over the whole experimental cycle. Images were captured as a function of delay time between the excitation laser and the backlight pulses such that the maximum gas bubble diameters formed around gold nanoparticles could be determined.

RESULTS

We have determined single laser pulse bleaching thresholds at 532 nm for aqueous 50, 100, 150, and 250 nm gold nanoparticle solutions. The concentrations were chosen sufficiently low (1.2×10^8 particles/mL) to avoid significant beam attenuation within the sample and still be able to detect the bleaching effect optically (i.e., elimination of the plasmon resonance absorption band near 532 nm). The bleaching laser pulse energy levels from the measurements are shown in Figure 2 alongside the results from the theoretical model described later in the text. The bleached region, which appears as a transparent clear solution, remains visible to the naked eye typically for a few seconds before the system becomes homogeneous again. In addition to the instant single pulse bleaching, a slower process occurring over many low intensity laser pulses (ca. 30% of the single pulse bleaching level) was also observed. This may be due to, for example, burning off of the surfactant[32] covering the particles leading to clustering or removal of the particles from the excitation volume by convective flow produced by heating of the solution. Particle fragmentation at these laser pulse energies was independently confirmed by DLS measurements. After 45 min of irradiation at the NP fragmentation threshold pulse energy, the DLS spectra showed broadening and shifting toward smaller particle sizes. This change is caused by reclustering events driven by the small fragments originating from the explosive boiling of the laser-heated NPs and the removal of the surfactant covering them. The raw DLS data before and after laser irradiation are provided as Supporting Information.

To study the gas bubble formation around individual gold nanoparticles, we have employed high-energy laser pulses, which are well above the particle fragmentation limit. A typical shadowgraph image following laser excitation of an aqueous gold nanoparticle sample is shown in Figure 3. The bubbles appear only after laser excitation and within the spatial laser beam volume. Since the focal depth of the imaging system is sharp, only particles appearing at the crossing of the beam volume and the focal plane are imaged. The bright spot appearing at the center of each bubble is due to the lensing effect where the backlight becomes focused due to the variation in the index of refraction at the gas−liquid interface of the bubble. This was deemed the most likely explanation as

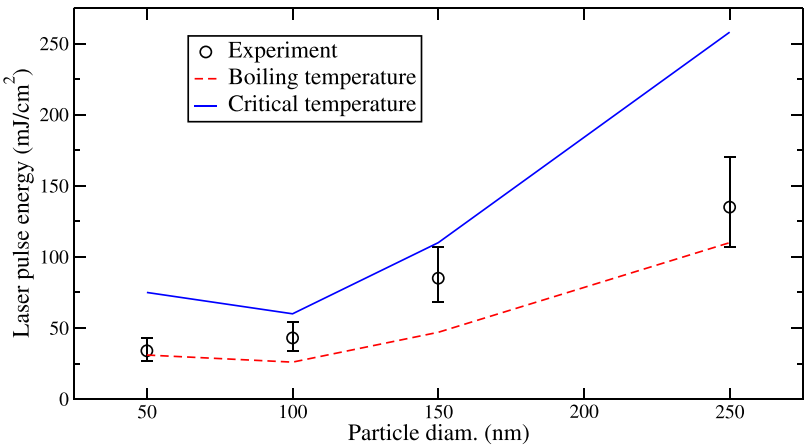

Figure 2. Laser pulse energy thresholds required to fragment gold nanoparticles (circles with error bars determined by the ND filter resolution; ambient pressure), boil the particles (red dashed line; theory), and reach the thermodynamic critical temperature of gold (blue continuous line; theory). Particle concentration 1.2×10^8 particles/mL.

https://dx.doi.org/10.1021/acs.jpcc.0c02637
J. Phys. Chem. C 2020, 124, 14022−14029

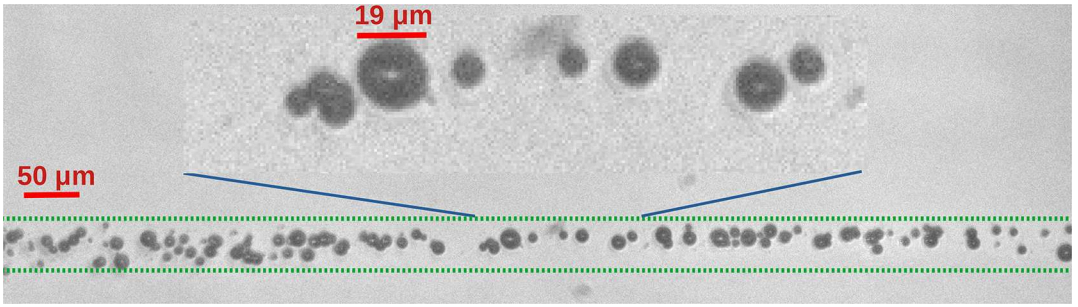

Figure 3. Representative shadowgraph image of 250 nm gold nanoparticles (1.9×10^8 particles/mL) recorded 1 μs after the excitation laser pulse (8000 mJ/cm^2) at 33 torr external pressure. The dotted green lines show the approximate laser beam edges (50 μm width). Magnification of the area identified by the continuous blue lines is shown as an inset at the top of the figure.

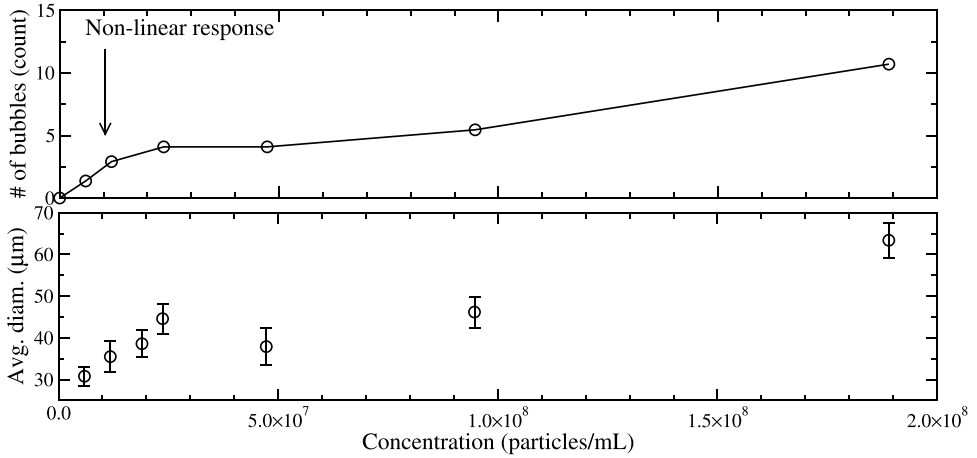

Figure 4. Top panel: Correlation between the number of gas bubbles observed in shadowgraph images recorded 10 μs after the excitation pulse and gold nanoparticle (250 nm) concentration. The concentration limit above which the relationship becomes nonlinear is indicated by an arrow. Bottom panel: The corresponding average bubble diameter as a function of concentration. Note that the bubbles appear nonspherical in the nonlinear response regime. Excitation laser pulse energy 20 500 mJ/cm^2 and external pressure 33 torr.

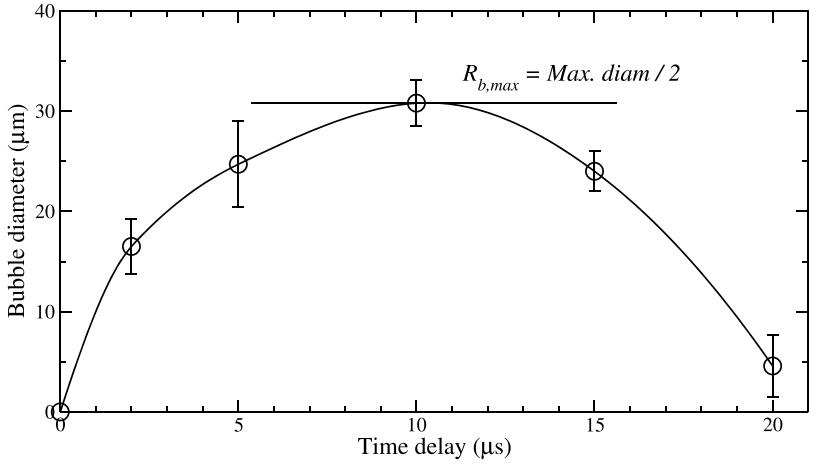

Figure 5. Average bubble diameter trajectory formed around 250 nm diameter gold nanoparticles at 33 torr external pressure. The maximum bubble diameter is identified by a horizontal line along with the resulting maximum bubble radius, $R_{b,max}$. The circles represent the data from measurements, and the continuous line corresponds to the spline curve fit. The error bars denote the standard deviation of the observed bubble diameters. At early times the bubble radius R_b increases approximately as $R_b \propto t^{1/3}$. Excitation laser pulse energy 20 500 mJ/cm^2 and particle concentration 5.9×10^6 particles/mL.

viewing gas bubbles during the degassing period of the experiment (laser off) reveals identical bright spots without the presence of gold nanoparticles. In general, this variation of index of refraction also produces the contrast in shadowgraph images.[29] To eliminate spontaneous gas bubble formation under reduced pressure, it is important to pump the samples for a sufficiently long time before performing the measurements (see the Experimental Section). The top panel of Figure 4 shows the correlation between the nanoparticle concentration and the average number of gas bubbles observed in the

https://dx.doi.org/10.1021/acs.jpcc.0c02637
J. Phys. Chem. C 2020, 124, 14022−14029

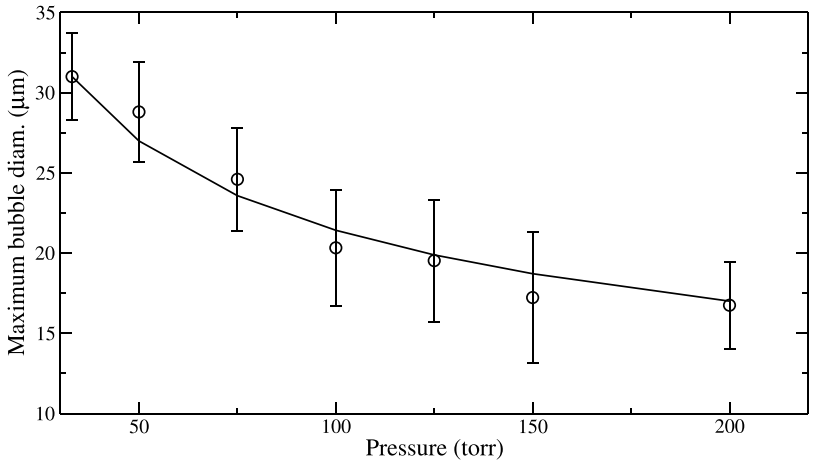

Figure 6. Dependence of maximum gas bubble diameter (μm) on external pressure (torr). Circles correspond to experiment and continuous line to theory (eq 4). The error bars denote the standard deviation of the observed bubble diameters. Excitation laser pulse energy 20 500 mJ/cm^2 and particle concentration 5.9 × 10^6 particles/mL.

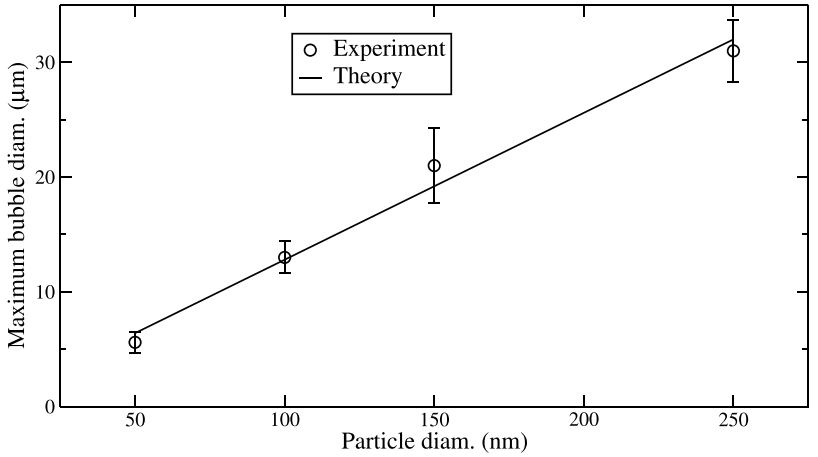

Figure 7. Dependence of maximum gas bubble diameter (μm) on gold nanoparticle size (nm) at 33 torr external pressure. Circles correspond to experiment and continuous line to theory (eq 1). The error bars denote the standard deviation of the observed bubble diameters. The data appear linear and can be fitted to a straight line: $y = 0.128x$. Excitation laser pulse energy 20 500 mJ/cm^2 and particle concentration 5.9 × 10^6 particles/mL.

shadowgraph frames. At low concentrations the relationship is linear, but after this the response levels off because the bubbles become spatially too close to each other and overlap, reducing the effective bubble number count. The bottom panel of Figure 4 shows the measured spherically averaged bubble diameters as a function of the particle concentration, which exhibits a similar trend as observed in the top panel. Since multiple bubbles coalesce in the high-concentration regime (i.e., beyond the nonlinear response arrow in the figure), the observed bubble size may not be the true bubble size. In this regime, the bubbles can become nonspherical and appear to have a larger effective size due to the coalescence of multiple bubbles.

To determine the maximum gas bubble diameter formed around the particles, we have recorded the average bubble diameter vs time profiles for each particle size. An example of such a trajectory is shown in Figure 5 for 250 nm particles, which was constructed by analyzing 250 individual shadowgraph images recorded as a function of time following the excitation laser pulse. By adjusting the pumping speed with the throttle valve, the maximum recorded bubble diameter was observed to decrease when the pressure inside the sample cuvette was increased as demonstrated in Figure 6. The average maximum bubble diameters observed at 33 torr external pressure for each particle size are plotted in Figure 7 along with the prediction from the theoretical model that is described later in the text. The bubble sizes were observed to be independent of laser pulse energy above 2000 mJ/cm^2 ("high pulse energy limit").

DISCUSSION

Laser−Particle Interaction Model. For nanosecond pulses, the electronic and nuclear temperatures remain approximately equal due to the large electron−phonon coupling.[33] This also implies that the thermal energy is distributed instantly in this time scale over the whole particle. Since the electronic heat capacity is much less than for phonons, we neglect the electronic contribution.[33,34] Furthermore, the radiative and conductive heat losses during the laser pulse are negligible. The former is slow compared to the duration of the laser pulse[8] whereas the heat conduction is greatly reduced by the dynamically appearing insulating Leidenfrost layer.[26] Within these assumptions the differential form of the thermodynamic model can be written as

https://dx.doi.org/10.1021/acs.jpcc.0c02637
J. Phys. Chem. C 2020, 124, 14022−14029

$$
\begin{aligned}
&dq_p = dq_{ex} \text{ when } T = T_m \text{ and } 0 \le q_p \le \Delta_{fus}H \\
&dq_p = dq_{ex} \text{ when } T = T_b \text{ and } \\
&\quad \Delta_{fus}H \le q_p \le \Delta_{fus}H + \Delta_{vap}H \\
&dq_r = dq_{ext} \text{ and } \quad dT = \frac{dq_r}{C_x} \text{ if none of the above apply} \\
&dq = dq_p + dq_r
\end{aligned} \tag{1}
$$

where T is the temperature, T_m is the melting temperature of gold, T_b is the boiling temperature, $\Delta_{fus}H$ is the fusion enthalpy, $\Delta_{vap}H$ is the vaporization enthalpy, q is the total heat absorbed by the particle, q_p is the heat used for driving phase transitions, q_r is the heat used for increasing the temperature of the particle, dq_{ex} is the heat delivered by the laser pulse (see below), and C_x is the heat capacity of gold for the current phase, x = s, l (solid or liquid). Since the particle sizes 50 nm or larger are used in this work, we can take the bulk values for these constants (see Supporting Information for ref 33.). Division of eq 1 by the time differential, dt, produces a set of differential equations that can be solved numerically.

The heat per particle introduced by the laser at a given point in time t is given by

$$
dq_{ex} = I_0 G(t) \sigma_{abs}(T) \tag{2}
$$

where I_0 is the laser pulse energy (J/m^2), $G(t)$ is the dimensionless temporal pulse profile function (normalized Gaussian with 5 ns fwhm), and $\sigma_{abs}(T)$ is the temperature-dependent absorption cross section (m^2). The latter quantity can be calculated using Mie theory.[28] The temperature dependence in the cross section arises from the possible change of the dielectric constant of the surrounding water (i.e., liquid vs gas).[27] We use the bulk liquid value below the boiling point of water (n = 1.33) and switch it to the gaseous surrounding (n = 1.00) when the water at the liquid−particle interface reaches boiling. This has been previously shown to occur at the spinodal decomposition temperature of water (573 K).[26] In practice, only the 50 nm particles were affected by this change in environment.

The gold nanoparticles were observed to fragment when their temperature became comparable to the thermodynamic critical temperature ($T_c \approx 7250$ K). Based on the bleaching data (see Figure 2) we have chosen the final particle temperature as $\approx 1/2T_c$. This determines the point where explosive boiling (or phase explosion) of the particle takes place.[24] We note that the peak power of our nanosecond laser is not sufficiently high to drive Coulomb explosion, which can be easily reached with femtosecond lasers.[35] After the sudden fragmentation into smaller particles, the contact surface area with the liquid increases rapidly, and consequently the heat conduction into the surroundings increases (i.e., breakdown of the originally formed Leidenfrost layer). This leads to vaporization of the liquid around each individual fragment and results in the formation of high-pressure water vapor that expands to produce a collective micrometer-scale gas bubble (*PV*-work) in the place where the particle was originally located. Since the small fragments transfer heat efficiently to the liquid, the process is dominated by *PV*-work (irreversible process), and the bubble radius formed can be related to the total amount of heat possessed by the original laser-heated nanoparticle:

$$
q \approx \frac{4\pi}{3} P_{ext} R_b^3 \tag{3}
$$

where q is the total heat absorbed by a single particle, P_{ext} is the external pressure, and R_b is the gas bubble radius. Note that surface tension work becomes negligible when the temperature of the surroundings exceeds the spinodal decomposition point of water (i.e., the explosive boiling regime of water). Furthermore, for particle sizes larger than 50 nm, the energy required for fragmenting the particles is estimated to be smaller than the *PV*-work.

Analysis of the Experimental Data. To analyze the single laser pulse bleaching thresholds using the above model, we determine the amount of laser-delivered energy required to heat the particles to a given temperature. A comparison between the experimental results and the model of eq 1 is shown in Figure 2. The data show that the final temperature for the particles falls between the boiling and critical temperatures of bulk gold. This final temperature for the particles appears independent of laser pulse energy above 2000 mJ/cm^2 indicating that the system becomes power saturated and phase explosion is already initiated during the laser pulse duration. Thus, the remainder of the pulse energy is not absorbed as the small fragments no longer exhibit a plasmon resonance band around 532 nm. The 50 nm particles show a slightly different trend due to the dynamic bleaching of the absorption cross section (i.e., changes in the dielectric environment). Despite this apparent difference in behavior, our data agree with the recent investigation of gold nanoparticle fragmentation in this size regime.[5]

To confirm that the source of the gas bubbles observed at high laser pulse energies (i.e., well above the fragmentation threshold) is due to solvated gold nanoparticles, we have verified that the bubbles appear only along the laser beam path after each pulse (see Figure 3) and correlated the number of gas bubbles observed with the gold nanoparticle concentration (see Figure 4). These data show that the bubbles observed in the shadowgraph images must appear around the gold nanoparticles rather than being formed spontaneously due to, for example, boiling under reduced pressure. Since the experiment employs repeated laser pulses above the bleaching threshold, the actual number of bubbles observed in each frame is fairly low. Particles that form bubbles around them along the beam path must have diffused (or moved by convection) back into the beam volume that was bleached by the previous laser pulse. Since the smaller particles appear less frequently in the images, their mobility appears to be reduced as compared to the larger ones. Although this experiment can provide the spatial locations of the nanoparticles in the solution, it is clearly destructive due to the resulting fragmentation. To minimize the perturbation of the sample, it is possible to carry out the measurement using a single laser pulse and a high-speed camera that can capture video frames in the microsecond time regime. As we have demonstrated earlier, modern machine-learning tools can be used to analyze such images efficiently by using computers.[30] The spatial locations of the particles can be most accurately determined at short delay times when the bubble diameters are small. In this case, the spatial accuracy at which the bubble position can be measured is limited by the optical resolution of the imaging system (in this work ±3 μm).

https://dx.doi.org/10.1021/acs.jpcc.0c02637
J. Phys. Chem. C 2020, 124, 14022−14029

To further confirm that the bubbles observed form around individual gold nanoparticles, their dynamic growth following the laser excitation was recorded (see Figure 5). Since the core of the bubble consists of many small gold particles, the bubble growth is not what is typically observed for cavitation bubbles. The initial scaling law shows an exponent of 1/3, which has been observed for large bubbles formed around multiple nanoparticles trapped on substrates.[3,4] Nevertheless, the data show clear growth, turnover point at maximum diameter, and the final collapse of the bubble. The maximum bubble diameter is an important parameter that allows estimating the amount of *PV*-work done. In accordance with eq 3, the bubble diameter is strongly affected by the external pressure. At atmospheric pressure, the bubbles become already smaller than our current optical resolution. Since the particles are excited with a laser pulse energy that greatly exceeds the fragmentation threshold, the resulting bubble sizes show almost no dependence on this parameter.

As shown in Figure 6, the maximum bubble diameter decreases as a function of the external pressure. This behavior is expected for pure *PV*-work and can be modeled by

$$D_b = \left(\frac{P_{ext,ref}}{P_{ext}}\right)^{1/3} D_{b,ref} \quad (4)$$

where $D_b = 2R_b$ is the bubble diameter at external pressure P_{ext}. $D_{b,ref}$ and $P_{ext,ref}$ are the corresponding quantities for a fixed reference state. The continuous line in Figure 6 corresponds to eq 4 with the first experimental point of the graph chosen as the reference: $P_{ext,ref}$ = 33 torr and $D_{b,ref}$ = 31 μm. This simple model clearly reproduces the experimentally observed pressure dependence. In fact, eq 4 is a variation of Boyle's law, which applies to any weakly interacting gaseous system.

In order to relate the observed maximum gas bubble size to the initial nanoparticle size, we set $R_b = R_{b,max}$ in eq 3 to provide an estimate for the maximum amount of *PV*-work done. As shown in Figure 7, the correlation between the presented thermodynamic model and the experimental data is very good. Thus, the presented method can provide not only the locations of the particles in the solution but also their individual sizes.

CONCLUSIONS

We have determined single laser pulse bleaching thresholds for aqueous gold nanoparticle solutions at 532 nm where the maximum particle temperatures were observed to reside between the boiling and critical temperatures of bulk gold. At laser pulse energies much higher than the bleaching limit, fragmentation of the particles was observed to lead to a rapid increase in heat conduction from the metal to the surrounding liquid (i.e., breakdown of the Leidenfrost layer) as evidenced by the formation of micrometer-scale gas bubbles at locations where the particles originally resided. The thermodynamic model presented in this work is able to provide temperature estimates for the laser-exposed particles as well as the sizes for the gas bubbles formed via pressure−volume work. In contrast to previously established methods such as DLS, UV/vis absorption spectroscopy, and X-ray scattering, the new method presented in this paper can determine both the locations and sizes of individual plasmonic nanoparticles in situ in the liquid phase. Although the measurement is destructive, the measurement can be performed using a single laser pulse that excites only a small volume in the liquid, leaving the majority of the system intact.

ASSOCIATED CONTENT

Supporting Information

The Supporting Information is available free of charge at https://pubs.acs.org/doi/10.1021/acs.jpcc.0c02637.

DLS data of gold nanoparticles before and after laser irradiation at the laser fragmentation threshold (PDF)

AUTHOR INFORMATION

Corresponding Author

Jussi Eloranta − *Department of Chemistry and Biochemistry, California State University at Northridge, Northridge, California 91330, United States;* orcid.org/0000-0002-0302-4329; Email: Jussi.Eloranta@csun.edu

Authors

Derek Stavich − *Department of Chemistry and Biochemistry, California State University at Northridge, Northridge, California 91330, United States*

Boris Nestoiter − *Department of Chemistry and Biochemistry, California State University at Northridge, Northridge, California 91330, United States*

Daniel Gonzalez − *Department of Chemistry and Biochemistry, California State University at Northridge, Northridge, California 91330, United States*

Adam Freund − *Department of Chemistry and Biochemistry, California State University at Northridge, Northridge, California 91330, United States*

Xavier Buelna − *Department of Chemistry and Biochemistry, California State University at Northridge, Northridge, California 91330, United States*

Kaiyue Wang − *Department of Chemistry and Biochemistry, California State University at Northridge, Northridge, California 91330, United States*

Joseph A. Teprovich, Jr. − *Department of Chemistry and Biochemistry, California State University at Northridge, Northridge, California 91330, United States;* orcid.org/0000-0002-7285-4844

Complete contact information is available at: https://pubs.acs.org/10.1021/acs.jpcc.0c02637

Notes

The authors declare no competing financial interest.

ACKNOWLEDGMENTS

Financial support from the National Science Foundation grant DMR-1828019 is gratefully acknowledged.

REFERENCES

(1) Jain, P. K.; Lee, K.-S.; El-Sayed, I. H.; El-Sayed, M. A. Calculated Absorption and Scattering Properties of Gold Nanoparticles of Different Size, Shape, and Composition. *J. Phys. Chem. B* **2006**, *110*, 7238−7248.

(2) Amendola, V.; Pilot, R.; Frasconi, M.; Marago, O. M.; Iati, M. A. Surface Plasmon Resonance in Gold Nanoparticles: A Review. *J. Phys.: Condens. Matter* **2017**, *29*, 203002.

(3) Wang, Y.; Zaytsev, M. E.; Lajoinie, G.; The, H. L.; Eijkel, J. C. T.; van den Berg, A.; Versluis, M.; Weckhuysen, B. M.; Zhang, X.; Zandvliet, H. J. W.; et al. Giant and Explosive Plasmonic Bubbles by Delayed Nucleation. *Proc. Natl. Acad. Sci. U. S. A.* **2018**, *115*, 7676−7681.

(4) Wang, Y.; Zaytsev, M. E.; The, H. L.; Eijkel, J. C. T.; Zandvliet, H. J. W.; Zhang, X.; Lohse, D. Vapor and Gas-Bubble Growth Dynamics Around Laser-Irradiated, Water-Immersed Plasmonic Nanoparticles. *ACS Nano* **2017**, *11*, 2045−2051.
(5) Fales, A. M.; Vogt, W. C.; Pfefer, J.; Ilev, I. K. Quantitative Evaluation of Nanosecond Pulsed Laser-Induced Photomodification of Plasmonic Gold Nanoparticles. *Sci. Rep.* **2017**, *7*, 15704.
(6) Lapotko, D. Optical Excitation and Detection of Vapor Bubbles Around Plasmonic Nanoparticles. *Opt. Express* **2009**, *17*, 2538−2556.
(7) Lukianova-Hleb, E.; Hu, Y.; Latterini, L.; Tarpani, L.; Lee, S.; Drezek, R. A.; Hafner, J. H.; Lapotko, D. O. Plasmonic Nanobubbles as Transient Vapor Nanobubbles Generated Around Plasmonic Nanoparticles. *ACS Nano* **2010**, *4*, 2109−2123.
(8) Takami, A.; Kurita, H.; Koda, S. Laser-Induced Size Reduction of Noble Metal Particles. *J. Phys. Chem. B* **1999**, *103*, 1226−1232.
(9) Jollans, T.; Orrit, M. Explosive, Oscillatory, and Leidenfrost Boiling at the Nanoscale. *Phys. Rev. E: Stat. Phys., Plasmas, Fluids, Relat. Interdiscip. Top.* **2019**, *99*, 063110.
(10) Baffou, G.; Quidant, R. Nanoplasmonics for Chemistry. *Chem. Soc. Rev.* **2014**, *43*, 3898−3907.
(11) Yang, J.; Li, Y.; Zu, L.; Tong, L.; Liu, G.; Qin, Y.; Shi, D. Concentrating Plasmonic Au Superstructures With Significantly Visible-Light-Enhanced Catalytic Performance. *ACS Appl. Mater. Interfaces* **2015**, *7*, 8200−8208.
(12) Robert, H. M. L.; Kundrat, F.; Bermudez-Urena, E.; Rigneault, H.; Monneret, S.; Quidant, R.; Polleux, J.; Baffou, G. Light-Assisted Solvothermal Chemistry Using Plasmonic Nanoparticles. *ACS Omega* **2016**, *1*, 2−8.
(13) Notarianni, M.; Vernon, K.; Chou, A.; Aljada, M.; Liu, J.; Motta, N. Plasmonic Effect of Gold Nanoparticles in Organic Solar Cells. *Sol. Energy* **2014**, *106*, 23−37.
(14) Polman, A. Solar Steam Nanobubbles. *ACS Nano* **2013**, *7*, 15−18.
(15) Emelianov, S. Y.; Li, P.-C.; O'Donnell, M. Photoacoustics For Molecular Imaging and Therapy. *Phys. Today* **2009**, *62*, 34−39.
(16) Shao, J.; Xuan, M.; Dai, L.; Si, T.; Li, J.; He, Q. Near-Infrared Activated Nanocalorifiers in Microcapsules: Vapor Bubble Generation for *In Vivo* Enhanced Cancer Therapy. *Angew. Chem., Int. Ed.* **2015**, *54*, 12782−12787.
(17) Wilks, J. *The Properties of Liquid and Solid Helium*; Clarendon Press: Oxford, U.K., 1967.
(18) Lombard, J.; Biben, T.; Merabia, S. Kinetics of Nanobubble Generation Around Overheated Nanoparticles. *Phys. Rev. Lett.* **2014**, *112*, 105701.
(19) Merabia, S.; Shenogin, S.; Joly, L.; Keblinski, P.; Barrat, J.-L. Heat Transfer From Nanoparticles: A Corresponding State Analysis. *Proc. Natl. Acad. Sci. U. S. A.* **2009**, *106*, 15113−15118.
(20) Hu, M.; Petrova, H.; Hartland, G. V. Invertigation of the Properties of Gold Nanoparticles in Aqueous Solution at Extremely High Lattice Temperatures. *Chem. Phys. Lett.* **2004**, *391*, 220−225.
(21) Kotaidis, V.; Dahmen, C.; von Plessen, G.; Springer, F.; Plech, A. Excitation of Nanoscale Vapor Bubbles at the Surface of Gold Nanoparticles in Water. *J. Chem. Phys.* **2006**, *124*, 184702.
(22) Wang, S.; Fu, L.; Xin, J.; Wang, S.; Yao, C.; Zhang, Z.; Wang, J. Photoacoustic Response Induced by Nanoparticle-Mediated Photothermal Bubbles Beyond the Thermal Expansion for Potential Theranostics. *J. Biomed. Opt.* **2018**, *23*, 1.
(23) Zhao, C.; Liu, Y.; Zhao, Y.; Fang, N.; Huang, T. J. A Reconfigurable Plasmofluidic Lens. *Nat. Commun.* **2013**, *4*, 2305.
(24) Karim, F.; Vasquez, E. S.; Sun, Y.; Zhao, C. Optothermal Microbubble Assisted Manufacturing of Nanogap-Rich Structures for Active Chemical Sensing. *Nanoscale* **2019**, *11*, 20589−20597.
(25) Karim, F.; Vasquez, E. S.; Zhao, C. Fabricated Nanogap-Rich Plasmonic Nanostructures Through an Optothermal Surface Bubble in a Droplet. *Opt. Lett.* **2018**, *43*, 334−336.
(26) Metwally, K.; Mensah, S.; Baffou, G. Fluence Threshold for Photothermal Bubble Generation Using Plasmonic Nanoparticles. *J. Phys. Chem. C* **2015**, *119*, 28586−28596.
(27) Lukianova-Hleb, E. Y.; Volkov, A. N.; Lapotko, D. O. Laser Pulse Duration is Critical for the Generation of Plasmonic Nanobubbles. *Langmuir* **2014**, *30*, 7425−7434.
(28) Fernandez, V.; Garcia, A.; Vossoughian, K.; Popov, E.; Garrett, S.; Eloranta, J. Laser Assisted Detection of Metal Nanoparticles in Liquid He-II. *J. Phys. Chem. A* **2015**, *119*, 10882−10886.
(29) Panigrahi, P. K.; Muralidhar, K. *Schlieren and Shadowgraph Methods in Heat and Mass Transfer*; Springer: New York, 2012.
(30) Sajjadi, S.; Buelna, X.; Eloranta, J. Application of Time-Resolved Shadowgraph Imaging and Computer Analysis to Study Micrometer-Scale Response of Superfluid Helium. *Rev. Sci. Instrum.* **2018**, *89*, 013102.
(31) Eloranta, J. *A Simplified C Programming Interface for Research Instruments*. Available on: http://github.com/jmeloranta/libmeas/, 2020.
(32) Niu, Z.; Li, Y. Removal and Utilization of Capping Agents in Nanocatalysis. *Chem. Mater.* **2014**, *26*, 72−83.
(33) Strasser, M.; Setoura, K.; Langbein, U.; Hashimoto, S. Computational Modeling of Pulsed Laser-Induced Heating and Evaporation of Gold Nanoparticles. *J. Phys. Chem. C* **2014**, *118*, 25748−25755.
(34) Delfour, L.; Itina, T. Mechanisms of Ultrashort Laser-Induced Fragmentation of Metal Nanoparticles in Liquids: Numerical Insights. *J. Phys. Chem. C* **2015**, *119*, 13893−13900.
(35) Werner, D.; Furube, A.; Okamoto, T.; Hashimoto, S. Femtosecond Laser-Induced Size Reduction of Aqueous Gold Nanoparticles: In Situ Pump-Probe Spectroscopy Investigations Revealing Coulomb Explosion. *J. Phys. Chem. C* **2011**, *115*, 8503−8512.

https://dx.doi.org/10.1021/acs.jpcc.0c02637
J. Phys. Chem. C 2020, 124, 14022−14029